Few-layer black phosphorus-on-MAPbI₃ for superb visible-light photocatalytic hydrogen evolution from HI splitting

Ran Li[a], Xitao Li[a], Jiaojiao Wu[a], Xinding Lv[a], Yan-Zhen Zheng[b,*], Zhijie Zhao[a], Xiaoqing Ding[a], Xia Tao[a,b,**], Jian-Feng Chen[a,b]

[a] *State Key Laboratory of Organic-Inorganic Composites, Beijing University of Chemical Technology, 15 Beisanhuan East Road, Beijing 100029, PR China*
[b] *Research Center of the Ministry of Education for High Gravity Engineering & Technology, Beijing University of Chemical Technology, 15 Beisanhuan East Road, Beijing, 100029, PR China*

ABSTRACT

Organic-inorganic perovskites like MAPbI₃ with excellent optoelectric properties have recently gained concerns in photocatalytic HI splitting. However, their achieved hydrogen evolution reaction (HER) rates are still insufficient. Herein, a 2D few-layer black phosphorus (BP) as cocatalyst was anchored on MAPbI₃ via electrostatic coupling. The resultant BP/MAPbI₃ is rather stable in HI solution during the whole photoreaction, yielding a superb HER rate of $3742 \, \mu mol \, h^{-1} \, g^{-1}$ under visible irradiation, which is two orders of magnitude higher than that of MAPbI₃-only, far higher than that of MAPbI₃/Pt and also shows the advanced HER performance among MAPbI₃ based systems. The remarkably boosted HER activity is thoroughly explored by optical/optoelectrochemical measurements, showing that BP can act as an electron promoter to trap electrons derived from MAPbI₃ through a type I heterojunction in the interface. This contributes to a new paradigm for high-efficiency photocatalysts by anchoring non-metal cocatalyst onto MAPbI₃ for solar energy conversion.

1. Introduction

Producing green hydrogen (H_2) fuel from renewable solar energy is proposed as a prospective approach to settle the global energy crisis and environmental pollution issues [1–3]. Photocatalytic H_2 evolution using diversified semiconductor photocatalysts has attracted considerable attention as a clean and sustainable technique for solar-to-H_2 conversion [4–6]. In view of the solar energy utilization, an ideal photocatalyst should possess a suitable optical bandgap and conduction band position to harvest the broad sunlight spectrum and transform the absorbed solar energy to H_2 fuel. Hybrid organic-inorganic perovskite e.g. methylammonium lead iodide perovskite (MAPbI₃) has great absorption coefficient (10^4-$10^5 \, cm^{-1}$), inherent optical bandgap (1.5 eV) that allow absorbing the visible light with wavelengths ranging from about 280 nm to 800 nm [7,8]. Additionally, MAPbI₃ exhibits excellent electronic properties such as ambipolar charge transport and long charge diffusion length ($\sim 25 \, \mu m$ in MAPbI₃ single crystals) and thus has advanced the power conversion efficiency of new-generation solar cells to over 20% in recent 10 years [7,9–13]. These attractive features indeed

enable MAPbI₃ to be a good candidate for photocatalytic HER, while its instability in aqueous solution poses a huge challenge to photocatalytic application. Recently, Park and coworkers have addressed this bottleneck by subtly establishing the dynamic balance of the dissolution and precipitation of MAPbI₃ in saturated hydroiodic acid (HI) aqueous solution and achieved visible light photocatalytic H_2 evolution from HI splitting [14]. However, in comparison with the conventional semiconductors, the observed HER rate of MAPbI₃ in aqueous HI solution in the absence or presence of Pt cocatalyst is rather low, probably originating from the serious recombination of photogenerated charges within MAPbI₃ nanocrystals at nanoscale domain. Recent research showed that electron transporters such as reduced graphene oxide (rGO) and TiO₂/Pt combined with MAPbI₃ photocatalyst was found to improve the charge transportation efficiency by fast extraction of the photogenerated electrons from MAPbI₃, and then participate the reduction of the protons to produce H_2. Accordingly, the photocatalytic HER rates of MAPbI₃ based composites were greatly improved as compared with MAPbI₃ alone [15,16]. This further provides guidance for promoting the photocatalytic H_2 evolution performance of hybrid

---

* Corresponding author at: State Key Laboratory of Organic-Inorganic Composites, Beijing University of Chemical Technology, 15 Beisanhuan East Road, Beijing 100029, PR China.
** Corresponding author at: Research Center of the Ministry of Education for High Gravity Engineering & Technology, Beijing University of Chemical Technology, 15 Beisanhuan East Road, Beijing 100029, PR China.
E-mail addresses: zhengyz@mail.buct.edu.cn (Y.-Z. Zheng), taoxia@mail.buct.edu.cn (X. Tao).

perovskite nanocrystals through charge transportation modulation.

2D BP as a direct band-gap-layered semiconductor has attracted great attention owing to its outstanding physical properties such as the great charge-carrier mobility, large surface area with abundant active sites, and thickness-dependent adjustable band gap (0.3–2.0 eV) [17–23]. These excellent performances enable BP to work as an efficient photocatalyst/cocatalyst/electrocatalyst for water splitting to produce H_2 and O_2. For instance, Majima et al. reported efficient and steady metal-free BP/CN (graphitic carbon nitride) nanohybrid with a type I heterojunction as the photocatalyst. In this heterojunction, BP acted as the electron recipient for stimulated CN under visible light illumination, restraining the recombination of the photogenerated charges in CN. Zhu and co-workers firstly demonstrated an efficient Z-scheme heterostructured $BP/BiVO_4$ as the photocatalyst for water splitting to produce H_2 and O_2 under visible light illumination. He et al. reported BP/MoS_2 nanosheets through the deposition of MoS_2 on BP nanosheets to alter electronic attributes for boosted HER activity in an acidic environment (0.5 M H_2SO_4) [24–26]. Based on the inherent nature and favorable optoelectric features of BP, together with its proven positive effect on optoelectric activity, we tentatively envision that BP may act as an electron promoter to trap photogenerated electrons derived from $MAPbI_3$, and thus inhibit the serious recombination of photogenerated charges for $MAPbI_3$ nanocrystals [27–29]. Worthy noted, few-layer 2D BP shows with abundant active sites favorable to photocatalytic HER activity [30–32] and excellent acid-proof stability in an anaerobic microenvironment [26,33]. In this context, we attempt to combine few-layer BP with $MAPbI_3$ to prepare a stable and efficient BP-on-$MAPbI_3$ photocatalyst for HER from HI splitting, which has yet to be reported up to now.

In this work, we report a heterostructured $BP/MAPbI_3$ in $MAPbI_3$-saturated aqueous HI solution system via an electrostatic coupling method (Fig. 1), and its implementation as a photocatalyst for H_2 production from HI splitting [34]. We demonstrate that few-layer BP nanoflakes can act as an electron promoter to trap photogenerated electrons derived from $MAPbI_3$ through a type I heterojunction in the interface of $BP/MAPbI_3$, and consequently debase the recombination efficiency of photogenerated electrons. As a consequence, the fabricated $BP/MAPbI_3$ photocatalyst can effectively produce H_2 under visible light ($\lambda \geq 420$ nm) illumination with a superb photocatalytic HER rate of 3742 μmol h^{-1} g^{-1}. Such a HER rate is two orders of magnitude higher than that of $MAPbI_3$-only (35 μmol h^{-1} g^{-1}), much higher than that of $MAPbI_3$/Pt (192 μmol h^{-1} g^{-1}) and also exhibits the advanced HER performance among hybrid perovskite based photocatalytic system. Moreover, the $BP/MAPbI_3$ photocatalyst is rather stable in $MAPbI_3$-saturated HI solution, with no obvious decrease of HER activity in the process of the whole photoreaction. Considering its high HER activity and excellent stability in HI solution, $BP/MAPbI_3$ heterostructure contributes to a new example of designing and preparing highly efficient hybrid perovskite photocatalysts.

2. Experimental section

2.1. Materials synthesis

2.1.1. Synthesis of $MAPbI_3$ and $MAPbI_3$-saturated aqueous HI solution

The $MAPbI_3$ photocatalyst was prepared as in previous research [14]. Firstly, 1 mol/L of MAI and PbI_2 with a molar ratio of 1:1 were dissolved in 5 ml of Gamma-butyrolactone (GBL), under stirring at 60 °C for 2 h. After that, the solution was recrystallized by heating at 100 °C for 8 h to obtain $MAPbI_3$ crystals. The crystals were washed for three times with ethyl acetate and ethyl ether, respectively, followed by desiccation in a vacuum oven at 60 °C for 6 h.

The $MAPbI_3$-saturated aqueous HI solution was prepared by adding 1 mol/L of $MAPbI_3$ in 30 ml of HI aqueous solution, in which the saturated HI solution was prepared by mixing 50 wt% H_3PO_2 and 57 wt% HI in a volume ratio of 1:5. The solution was stirred at 60 °C for 2 h and cooled down to room temperature to acquire the $MAPbI_3$-saturated aqueous HI solution. The supernatant liquid of solution was sampled for the following experiments.

2.1.2. Synthesis of BP nanoflakes

The BP nanoflakes were prepared by using N-methyl pyrrolidone (NMP) solvent exfoliation, as shown in Fig. S1 [35,36]. 15 mg of bulk BP was ground in a mortar for 0.5 h and then added into 15 ml of NMP solvent. The samples were sonicated for 10 h at a power of 400 W, followed by centrifugation at 3000 rpm for 30 min to dislodge the non-exfoliated BP bulk. After that, the supernatant was centrifuged at 9500 rpm for 1 h to obtain the precipitate. The precipitate was washed with methanol and ethyl ether, respectively, followed by drying in a vacuum oven at 60 °C for 6 h.

2.1.3. Synthesis of $BP/MAPbI_3$ composites

We adjust the proportion of samples, aiming at achieving the optimal-performance composite photocatalysts. As such, we carried out a series of experiments on measuring photocatalytic HER rates of composites including $BP/MAPbI_3$ and BP bulk/$MAPbI_3$, and consequently determine the suitable proportion range with an optimal HER performance. Specifically, the BP dispersion was first prepared by adding 1 mg/ml BP nanoflakes to the $MAPbI_3$-saturated aqueous HI solution. Then the BP dispersion (0.6, 1.2, 1.8, 2.4, 3, 3.6 and 4.2 ml) and 200 mg of $MAPbI_3$ were added to the $MAPbI_3$-saturated HI aqueous solution. The $BP/MAPbI_3$ photocatalyst was obtained by electrostatic adsorption of BP nanoflakes on the surfaces of $MAPbI_3$ during the precipitation-crystallization cycle. The composite photocatalyst was rinsed and dried for further characterizations.

For parallel comparison of photocatalytic HER activity, the BP bulk/$MAPbI_3$ composites were also prepared by adding 50 mg of $MAPbI_3$ and BP bulk (0.5, 1, 1.5, 2, 2.5, 3, 3.5 and 4 mg) to the prepared $MAPbI_3$-saturated aqueous HI solution to obtain BP bulk/$MAPbI_3$ photocatalysts with various amounts of BP bulk.
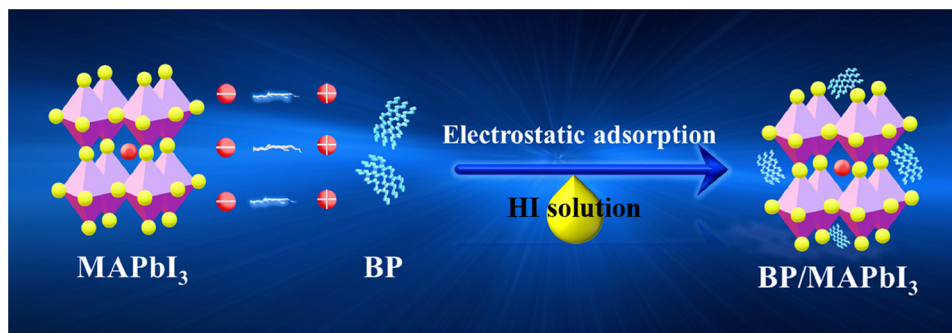

Fig. 1. Schematic diagram of the preparation process of $BP/MAPbI_3$ photocatalyst.

2.2. Characterizations

X-ray power diffraction (XRD) patterns were detected using Cu Ka radiation ($\lambda = 0.15406$ nm) on a Rigaku D/max-2500 VB2+/PC in the 2θ range 10-70° at a scanning rate of 5°/min to characterize the crystalline structure of samples. The photocatalyst morphology was observed by scanning electron microscopy (SEM) images on a Hitachi S-4700 microscope and transmission electron microscopy (TEM) images of samples were performed on a Hitachi 7700 microscope. An energy-dispersive spectroscopy (EDS) measurement was performed with an X-ray energy dispersive spectrometer installed on a JEOL-6701 F microscope. High resolution transmission electron microscopy (HRTEM) images were surveyed by a Hitachi H-9500 microscope. X-ray photoelectron spectroscopy (XPS) data was conducted on a thermo ESCALAB250 surface analysis system using Al Kα X-ray source. Atomic force microscope (AFM) images were received from Bruker Multimode 8 with ScanAsyst scanning probe microscope using Bruker SNL-10 probes. The Brunauer-Emmett-Teller (BET) specific surface area was tested through Quantachorme Quadrasorb SI instrument. The photoluminescence (PL) spectra and time-resolved PL decay spectra were characterized by using a Spectrofluorometer FS5 (EDINBURGH INSTRUMENTS) with an excitation wavelength of 347 nm at RT. The optical property of samples was obtained by using UV–vis spectrophotometry (Lambda 950, Perkin Elmer). Kelvin Probe Force Microscopy (KPFM) measurement was carried out on atomic force microscope (Broker, multimode 8) with Pt/Ir-coated tip and the cantilever coated with Au was used for modes.

2.3. Photocatalytic H$_2$ evolution

The photocatalytic HER experiments in aqueous HI solution were executed in a 15 ml cylindrical quartz reactor. The source of the photocatalytic reaction was a 300 mW cm^{-2} Xe lamp (Beijing China Education Au-Light Technology Co., Ltd, CEL-HXF300) with a visible light ($\lambda \geq 420$ nm) illumination. 30 mg of BP/MAPbI$_3$ photocatalyst with different BP contents was added into 10 ml saturated HI solution containing 20 vol% H$_3$PO$_2$. The reactor was thoroughly degassed with N$_2$ for 15 min to remove air before irradiation, which would further guarantee the stability of BP immersed into an almost anaerobic HI solution (the less oxygen content implies the more stable BP) [37]. The generated H$_2$ was detected by gas chromatography (7890 B GC System, Agilent Technologies) with high-purity nitrogen carrier gas. Note that five independent H$_2$ production experiments for each batch sample were conducted in parallel.

The apparent quantum efficiency (AQE) was surveyed by using band-pass filters (420, 500, 550, 600 and 800 nm) for 1 h. The illumination area was ~ 0.25 cm^2 and the average intensities of irradiation at 420, 500, 550, 600 and 800 nm were determined to be 25.3, 23.9, 22.4, 18.7 and 14.6 mW cm^{-2}, respectively. After that, we calculated the AQE at different excitation wavelengths [38,39].

The solar HI splitting efficiency of BP/MAPbI$_3$ in saturated HI solution without H$_3$PO$_2$ was surveyed by Xe lamp with a 420 nm cutoff filter. The average intensity of irradiation was fixed as 100 mW cm^{-2} in this case. The standard hydrogen reduction potential and I$^-$ oxidation potential to I$_3^-$ was 0 V (versus RHE) and 0.53 V (versus RHE), respectively. The concentration of HI in solution was 7.44 mol L^{-1}. The I$_3^-$ concentration was estimated as 1.72×10^{-3} M by analyzing UV–vis absorption spectrum of HI aqueous (Fig. S2) and using the following equation [14]:

$$y = 0.0293x + 0.00299$$

where y is the value of the absorbance at 353 nm, x is the concentration of I$_3^-$.

Based on the above results, we calculated that E(2H$^+$ + 2e$^-$ → H$_2$) = 0.051(versus NHE) and E(3I$^-$ → I$_3^-$ +

2e$^-$) = 0.371(versus NHE). Thus, the total potential for the HI solution splitting could be computed as 0.371 V − 0.051 V = 0.320 V. By using this potential, we estimated the solar HI splitting efficiency based on the amount of evolved H$_2$ [40,41].

2.4. Photoelectrochemical (PEC) measurements

The PEC performance was detected in a standard three-electrode configuration with a certain MAPbI$_3$-saturated aqueous HI solution, the Pt wire and saturated calomel electrode used as the counter electrodes and reference electrode, respectively. As for working electrode, it was based on a plasma treated indium-tin oxide (ITO). Firstly, the ITO was washed with deionized water and absolute ethanol respectively, followed by treating under UV-ozone for 20 min. 200 mg of BP/MAPbI$_3$ was dispersed in chlorobenzene and ultrasound for 15 min, and the dispersion was suspended on ITO glass and annealed at 80 °C for 20 min under nitrogen atmosphere to obtain photoelectrode. The source for the PEC performance was a 300 mW cm^{-2} Xe lamp with a visible light ($\lambda \geq 420$ nm) illumination. All electrochemical performance assays were performed at ambient environment.

3. Results and discussion

3.1. Structure, composition and optical property of BP nanoflakes and BP/MAPbI$_3$ photocatalyst

The few-layer BP nanoflakes were prepared by using NMP solvent exfoliation, as shown in Fig. S1. To explore the morphology and thicknesses of as-prepared BP nanoflakes, we performed AFM and TEM characterization of BP samples. The thicknesses of the exfoliated BP nanoflakes were measured to range from 7 to 20 nm (Fig. 2a), corresponding to the 10–40 phosphorusatomic layers based on the monolayer thickness of 0.5-0.7 nm [42]. Additionally, few-layer sheet-like structure of BP nanoflakes with the size of ~ 400 nm is observed from TEM image (Fig. 2b). Worthy noted, to detect the structural stability of BP, the XRD spectra of BP samples before and after immersing in HI aqueous solution were measured, and found that BP is rather stable in HI aqueous solution (Fig. 2c).

The BP/MAPbI$_3$ photocatalysts were prepared by electrostatic adsorption of positively charged BP nanoflakes (16.7 mV) on the surface of the negatively charged MAPbI$_3$ (-20.1 mV) in HI aqueous solution (Figs. 1 and S3). XRD patterns (Fig. 3) show that the fabricated MAPbI$_3$ is tetragonal crystal structure with the characteristic diffraction peaks centered at 14.1, 28.4, 31.8, 40.4, and 43.0°, respectively [15]. No characteristic diffraction peaks of BP can be found in the XRD pattern of the BP/MAPbI$_3$ because of a trace amount of BP nanoflakes [31].

To clarify the interfacial interaction between BP and MAPbI$_3$ in BP/MAPbI$_3$, (HR-)TEM and SEM images, and corresponding EDS elemental mapping were characterized. As shown in Fig. 4a, the large MAPbI$_3$ particles are tightly packed on the BP nanoflakes because of the electrostatic adsorption at their interface. Moreover, considering that the size of MAPbI$_3$ is much larger than that of BP nanoflakes, we performed HRTEM assays by focusing on different zones within the same area. As shown in Fig. 4b, clear lattice fringes with a d-spacing of 0.356 nm are consistent with the (220) planes of MAPbI$_3$ [15]. From Fig. 4c, clear lattice fringes with d-spacing of 0.280 nm and 0.217 nm are observed, matching to the (040) and (002) plane of BP nanoflakes, respectively [42]. EDS element mapping (Fig. 5a–d) presents a uniform distribution of P, Pb, and I on the BP/MAPbI$_3$ composite. The atomic ratio of P:Pb:I of 1.2% BP/MAPbI$_3$ is determined as 1:3.71:12.18 (Fig. S4). The S$_{BET}$ of 1.2% BP/MAPbI$_3$ was determined to be 10.5 m^2 g^{-1}.

To further explore the surface chemical states of the BP/MAPbI$_3$ composite, XPS spectra were measured. The XPS full scan spectrum of BP/MAPbI$_3$ (Fig. 6a) clearly shows the existence of the binding energy peaks of P 2p, Pb 4f, I 3d, and C 1s. The high resolution XPS spectrum of P 2p (Fig. 6b) in BP/MAPbI$_3$ could be deconvoluted into three peaks
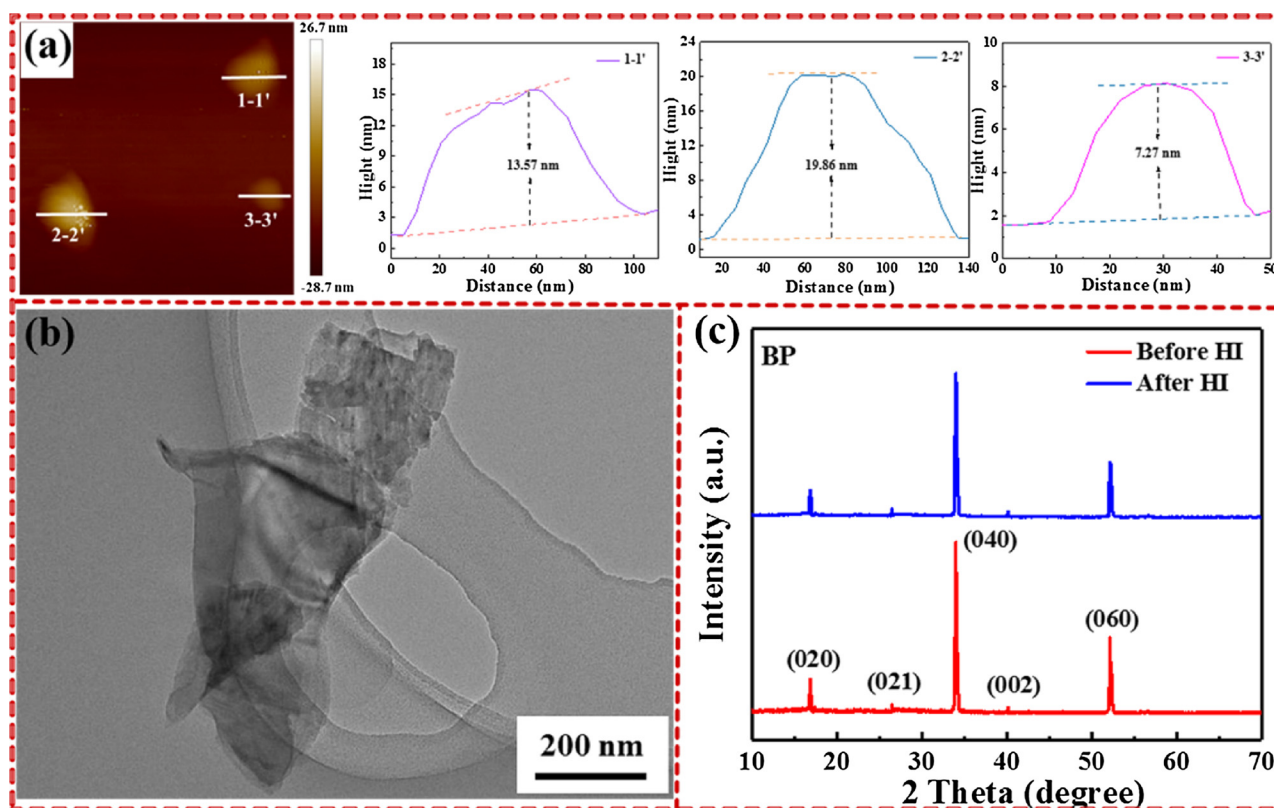
Fig. 2. (a) Typical AFM image and the corresponding measured thicknesses of BP nanoflakes, (b) TEM image of BP nanoflakes, (c) XRD patterns of BP nanoflakes before and after immersing in HI aqueous solution for 7 days.
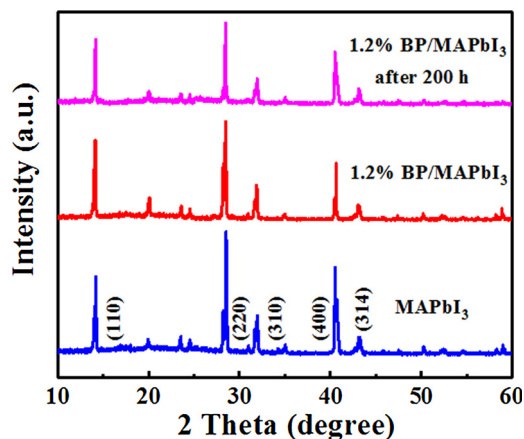

Fig. 3. XRD patterns of MAPbI$_3$, and 1.2% BP/MAPbI$_3$ before and after 200 h-photocatalytic H$_2$ evolution experiment.

located at 129.7, 130.4, 134.1 eV, corresponding to P 2p$_{3/2}$ and P 2p$_{1/2}$ of elemental P^0 as well as P 2p of oxidized P$_x$O$_y$, respectively [24,42]. The high resolution XPS spectrum of I 3d (Fig. 6c) in BP/MAPbI$_3$ could be deconvoluted into two peaks located at 618.9 and 630.5 eV, corresponding to I 3d$_{5/2}$ and I 3d$_{3/2}$, respectively. The high resolution XPS spectrum of Pb 4f (Fig. 6d) in BP/MAPbI$_3$ can be deconvoluted into two peaks located at 138.3 and 143.2 eV, corresponding to Pb 4f$_{7/2}$ and P 2p$_{5/2}$. It should be noticed that the binding energies of I 3d and Pb 4f in BP/MAPbI$_3$ are both 0.2 eV larger than those in pristine MAPbI$_3$ (Fig. 6c &d), probably due to the migration of electron density from MAPbI$_3$ phase to BP phase. This indicates the intimate interaction between MAPbI$_3$ and BP in the composite [43,44]. The optical property of the BP/MAPbI$_3$ was analyzed by UV–vis diffuse reflectance spectra, as shown in Fig. 7. Apparently, loading BP nanoflakes onto the surface of

MAPBI$_3$ can increase the absorption in the visible light region ranging from 400 to 850 nm with the increase of BP amount (0, 0.6, 1.8, 2.4%), which is expected to be beneficial to photocatalytic HER.

3.2. Photocatalytic HER activities

The photocatalytic HER activities of as-prepared BP/MAPbI$_3$ composites were investigated in MAPbI$_3$-saturated aqueous HI solution under visible light ($\lambda \geq 420$ nm) illumination with H$_3$PO$_2$ as sacrificial reagent. Fig. 8a shows the photocatalytic HER activities of MAPbI$_3$ and BP/MAPbI$_3$ with various amounts of BP nanoflakes cocatalyst (0.3, 0.6, 0.9, 1.2, 1.5, 1.8 and 2.1%). A trace amount of H$_2$ (35 µmol h^{-1} g^{-1}) is detected when only use pure MAPbI$_3$ photocatalyst owing to its rapidly recombination of photogenerated electrons. On the other hand, when use BP/MAPbI$_3$ composite photocatalyst, the HER activity for HI splitting is greatly boosted. Moreover, with the increase of the loading amount of BP nanoflakes, the HER rate firstly increases and then decreases, with the optimum value of 3742 µmol h^{-1} g^{-1} at 1.2% loading amount of BP (Fig. 8a). Such a HER rate is 106-fold higher than that of MAPbI$_3$ (35 µmol h^{-1} g^{-1}), and 18-fold higher than that of Pt/MAPbI$_3$ (192 µmol h^{-1} g^{-1}), respectively, demonstrating the positive role of BP nanoflakes in the photocatalytic system of BP/MAPbI$_3$. For comparison, BP bulk with a variety of amount as cocatalyst combines with MAPbI$_3$ to examine the photocatalytic HI splitting performance of BP bulk/MAPbI$_3$ (Fig. S5). The highest H$_2$ evolution rate of BP bulk/MAPbI$_3$ is measured to be 584 µmol h^{-1} g^{-1} at 5% loading amount of BP bulk.

The distinct difference in photocatalytic H$_2$ evolution rates between BP/MAPbI$_3$ and BP bulk/MAPbI$_3$ is believed to be due to the positive effect of exfoliated few-layer BP. Note that H$_2$ evolution performances of perovskite-based photocatalysts including our prepared BP/MAPbI$_3$ and the other reported perovskite photocatalysts are compared and listed in Table S1. It can be found that our homemade BP/MAPbI$_3$ is superior to other photocatalysts. Further detailed exploration and
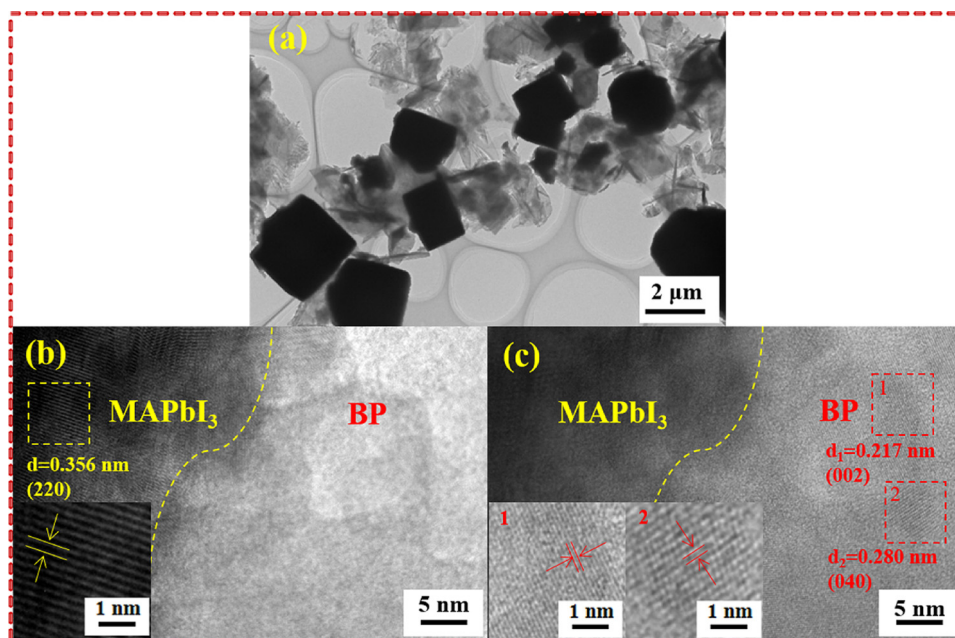
Fig. 4. TEM (a) and HRTEM (b&c) images of BP/MAPbI$_3$. Inset of (b) and (c) showing the magnified images of MAPbI$_3$ and BP nanoflakes, respectively.

explanation concerning the enhanced HER performance of BP/MAPbI$_3$ will be discussed in the following section.

Furthermore, the excellent photocatalytic HER activity of BP/MAPBI$_3$ can also be demonstrated through the AQE data (Fig. 8b). The AQE data for 1.2% BP/MAPbI$_3$ at 420, 500, 550, 600 and 800 nm were evaluated to 23.2%, 21.7%, 22.9%, 21.3% and 4.7%, respectively. Such a trend of AQE is observed to be consistent with that of UV–vis absorption spectrum of 1.2% BP/MAPbI$_3$ sample [45,46]. Besides, the HI splitting efficiency of 1.2% BP/MAPbI$_3$ was measured as 0.93% under visible light irradiation (see experimental section for details).

The photocatalytic HER stability test results as shown in Fig. 8c indicate that the BP/MAPbI$_3$ has superior durability showing no obvious decline in the activity of H$_2$ evolution in the continual 20-cycle repeated experiments (5 h for each cycle) and another 20 cycles after stored in HI solution for one month. The crystal structure of the BP/MAPbI$_3$ after photocatalytic H$_2$ evolution for 200 h is also re-examined and given in Fig. 3. Obviously, XRD patterns of BP/MAPbI$_3$ after photocatalytic cycling experiment have no phase change or structural degradation, further confirming the good photostability of the BP/MAPbI$_3$.
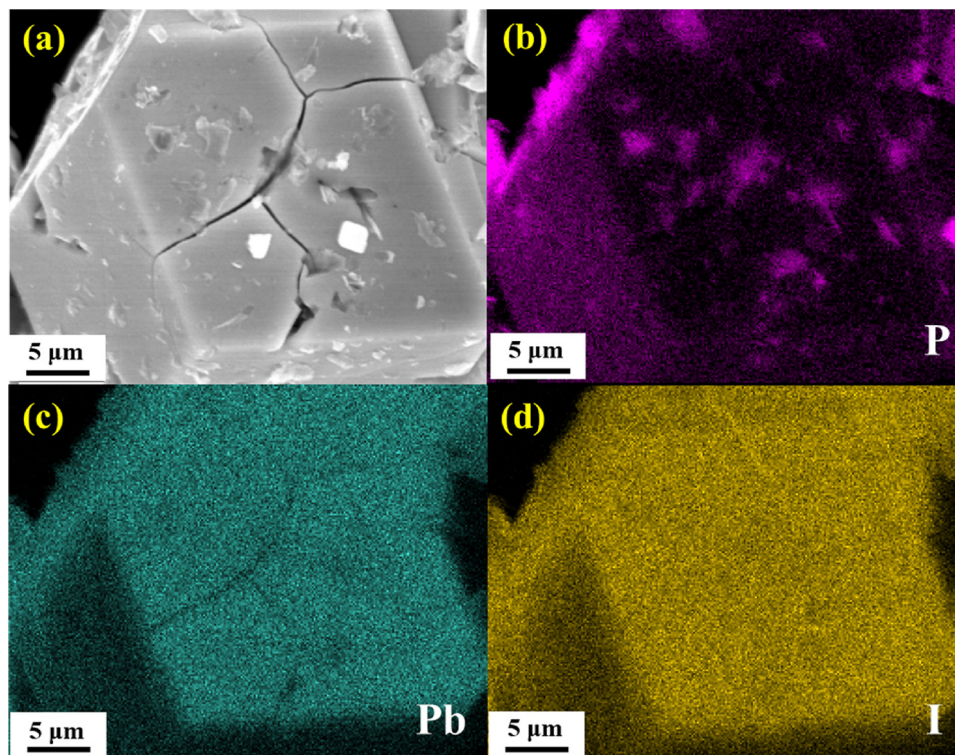

Fig. 5. SEM image (a) and the corresponding EDS elemental mappings of P (b), Pb (c), and I (d) of 1.2% BP/MAPbI$_3$.
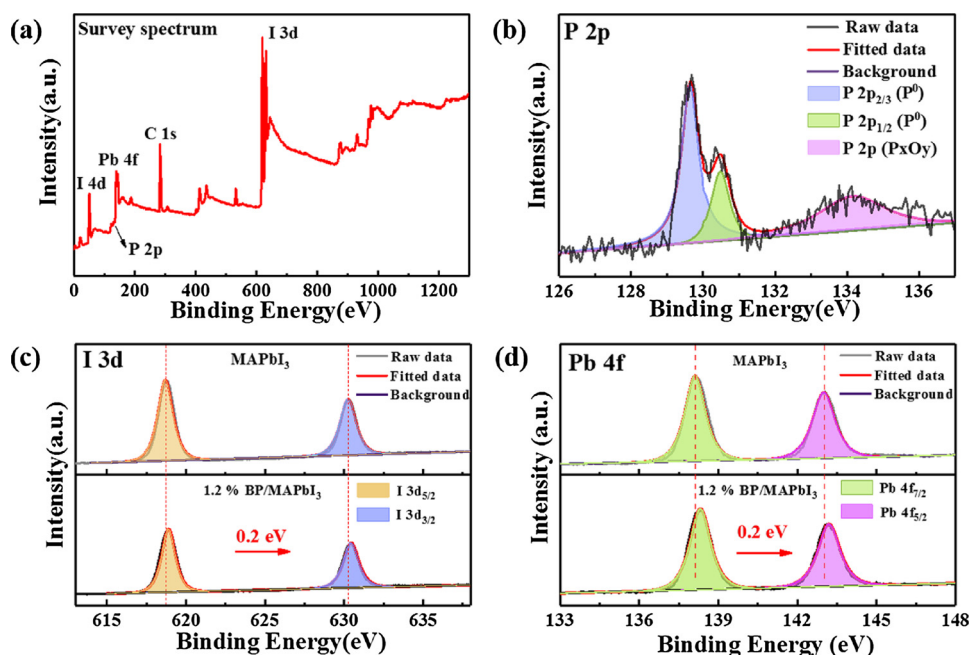
Fig. 6. XPS Survey spectrum (a), and high-resolution XPS spectra of P 2p (b), I 3d (c) and Pb 4f (d) in MAPbI$_3$ and 1.2% BP/MAPbI$_3$, respectively.
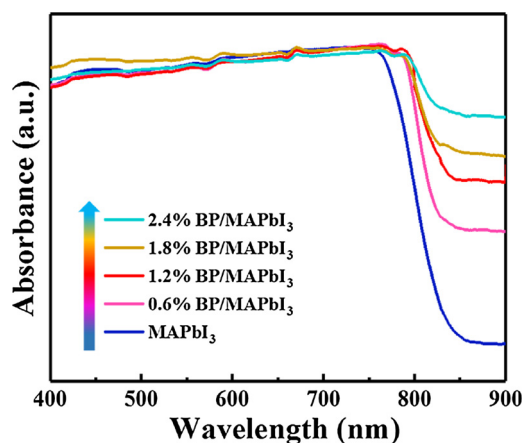

Fig. 7. UV–vis absorption spectra of BP/MAPbI$_3$ photocatalysts containing different amounts of BP nanoflakes (0, 0.6, 1.2, 1.8, and 2.4 wt%).

3.3. Origin and analysis of the enhanced performance

To explore the BP role in this distinct enhanced photocatalytic HER activity over MAPbI$_3$, we performed a series of supplementary PEC measurements [39]. The PEC analysis is widely used to provide efficient evidence for the electron-hole pair separation and transfer in the composite photocatalysts. As shown in I–V curves of Fig. 9a, the BP/MAPbI$_3$ photocatalyst shows the onset overpotential of 642 mV, which is lower than that of the pure MAPbI$_3$ with the value of 780 mV at a current density of 6 mA cm^{-2}, confirming more favorable electrocatalytic HER kinetics at the BP/MAPbI$_3$ [26,42,47]. The time-dependent photo-current responses for the pure MAPBI$_3$ and BP/MAPbI$_3$ under several 20 s on/off visible illumination cycles are performed and displayed in Fig. 9b. Specifically, in the case of illumination, the photocurrent intensity remains substantially unchanged, and it reduces to zero when the light turns off, revealing a fast photocurrent response to the on − off intermittent illumination [48–50]. Moreover, the high photocurrent intensity of BP/MAPbI$_3$ in comparison to pure MAPbI$_3$ indicates the efficient separation of the excited charge carriers at the interface of BP and MAPbI$_3$. Besides, EIS Nyquist plots was also

detected to obtain further investigation of the electrode kinetics during catalytic process (Fig. 9c). The semicircular diameter of the BP/MAPbI$_3$ (60 Ω) is observed to be smaller than that of the MAPbI$_3$ (140 Ω) electrode, revealing the outstanding roles of BP as cocatalyst to accelerate the charge transport and separation in the MAPbI$_3$ crystal matrix [51]. All above PEC results including I–V, time-dependent photocurrent responses as well as EIS demonstrate the increased charge conductivity and efficient separation of photogenerated carriers originating from exfoliated few-layer BP, and hence leading to the enhanced HER activity.

To further clarify the photogenerated charge separation and transport efficiency of the BP/MAPbI$_3$, photoluminescence (PL) spectra were also characterized. As shown in Fig. 10a, pure MAPbI$_3$ exhibits a strong emission because of the rapid recombination of photo-excited charges. After loading BP, the PL emission peak intensity drastically decreases, indicating that BP loading accelerates the charge carrier transfer in BP/MAPbI$_3$ [52,53]. Time-resolved PL spectra (TR-PL) provide the specific charge carrier decay kinetics in BP/MAPbI$_3$, as shown in Fig. 10b. PL lifetimes of BP/MAPbI$_3$ and MAPbI$_3$ are obtained by fitting biexponential kinetics function [54,55]. As shown in the Table S2, τ_1 and τ_2 reflect the nonradioactive recombination of charge carriers and the recombination of free excitons in the MAPbI$_3$, respectively. From the fitting results, we can see that the decay times for BP/MAPbI$_3$ ($\tau_1 = 7.0$ ns, $\tau_2 = 76.1$ ns) are much shorter than those of corresponding MAPbI$_3$ components ($\tau_1 = 37.6$ ns, $\tau_2 = 184.2$ ns). Based on the fitting data, the τ_{avg} value of BP/MAPbI$_3$ (74.7 ns) reduces significantly as compared with that of pure MAPbI$_3$ (180.2 ns) [54,55]. The quenching PL and decreasing lifetime imply that the photogenerated electron transfer from MAPbI$_3$ to BP is accelerated via a facile nonradiative quenching channel, beneficial for enhanced charge separation of electron-hole pairs and a high photocatalytic HER activity.

To seek for the electron transfer pathway in the BP/MAPbI$_3$ composite, we first probed the difference surface potentials between Pt/Ir-coated tip and samples (i.e. BP and MAPbI$_3$) by KPFM, and then analyzed their respective work function (WF) [56]. As shown in Fig. S6, the WF of BP and MAPbI$_3$ are calculated to be 4.28 and 4.34 eV, respectively. Besides, from the XPS valence-band spectra (Fig. S7), the valence-band positions (E$_{VB}$) of BP and MAPbI$_3$ are estimated to be 0.82 eV and 1.04 eV, respectively [38,56]. By virtue of the formula $E_{VB}^{NHE}/V = WF + E_{VB} - 4.44$ reported in the literature [57], together with
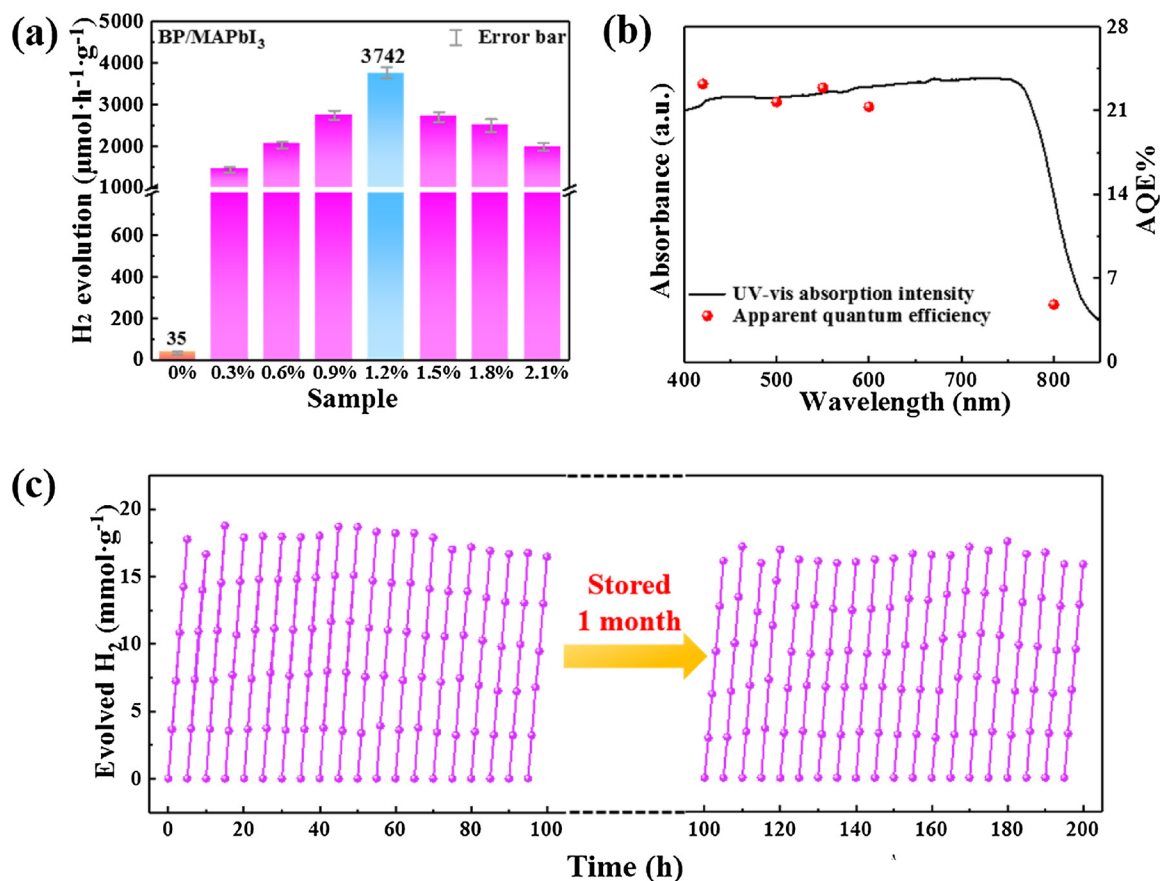
Fig. 8. (a) Photocatalytic H_2 evolution rates of $BP/MAPbI_3$. (b) Wavelength-dependent AQE and UV–vis absorption spectrum and (c) cycling tests of photocatalytic H_2 evolution over 1.2% $BP/MAPbI_3$.
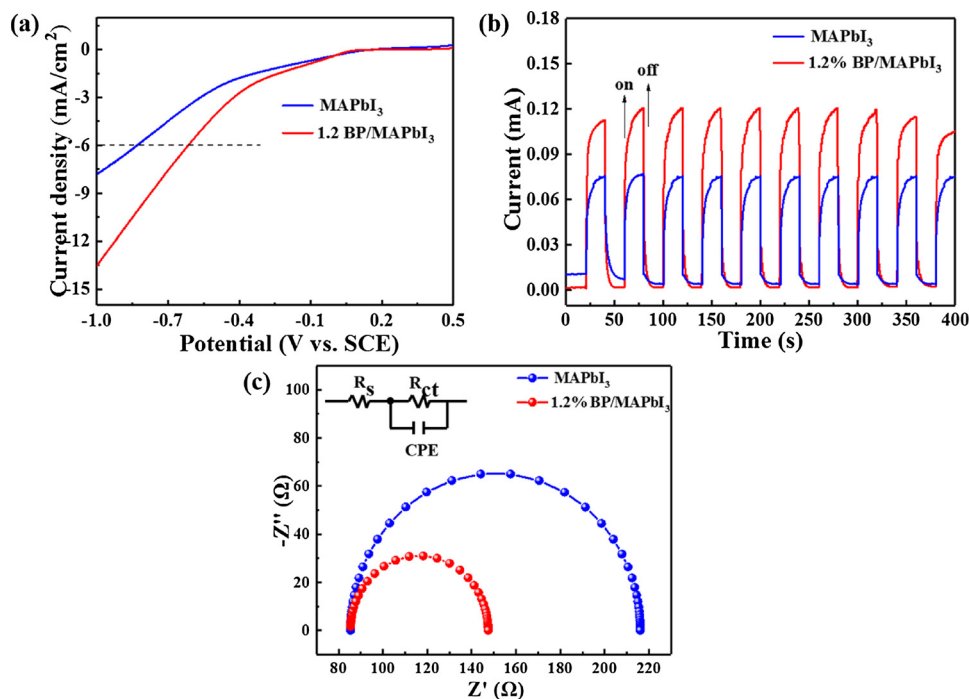

Fig. 9. (a) I–V curves, (b) visible light ($\lambda \geq 420\,nm$) induced transient photocurrent responses, and (c) EIS Nyquists plots of $MAPbI_3$ and $BP/MAPbI_3$.
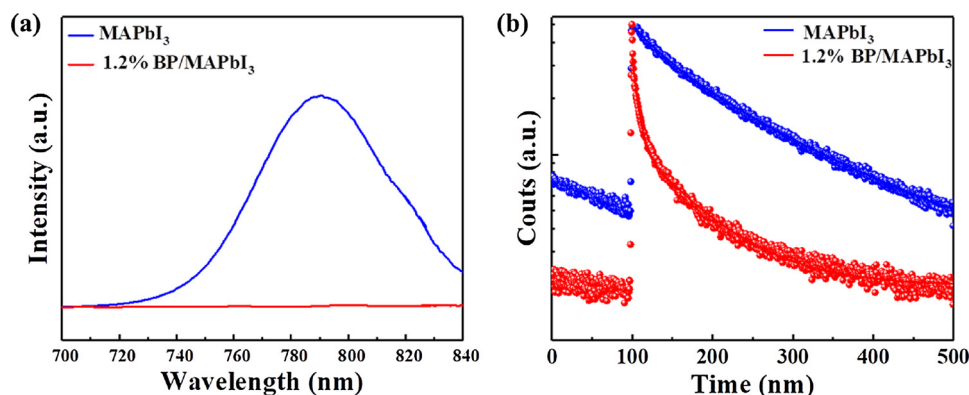
Fig. 10. (a) Steady-state PL and (b) time-resolved PL spectra of $MAPbI_3$ and $BP/MAPbI_3$.
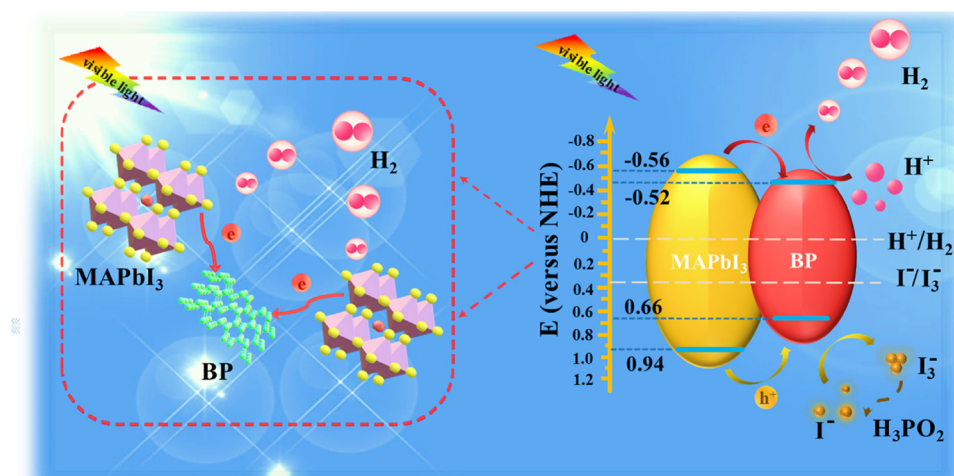

Fig. 11. Schematic illustration of the photogenerated charge transfer in the $BP/MAPbI_3$ under visible light ($\lambda \geq 420$ nm) illumination.

the obtained WF and E_{VB} values, the VB positions (E_{VB}^{NHE}) of BP and $MAPbI_3$ against the NHE can be calculated to be ~ 0.66 V for BP and 0.94 V for $MAPbI_3$. Based on E_{VB}^{NHE} and the bandgap energies (E_g) of BP ($E_g = 1.18$ eV) and $MAPbI_3$ ($E_g = 1.50$ eV) obtained by UV–vis absorption spectra (Figs. S8–9), the conduction band positions (E_{CB}^{NHE}) then are calculated to be -0.52 V for BP and -0.56 V for $MAPbI_3$, respectively [58].

In terms of the electronic band structures, a type I heterojunction at the interface of BP and $MAPbI_3$ is proposed, and the visible light photocatalytic HER process over $BP/MAPBI_3$ is schematically illustrated in Fig. 11 [24,59]. According to the H_2 evolution "band matching" theory, the CB potential level of $MAPbI_3$ is more negative than that of BP so that photo-generated e^- could migrate from $MAPbI_3$ to BP driven by the contact electric field, which facilitates the effective extraction of electrons for reduction of the proton to generate H_2 [60,61]. While the VB potential level of $MAPbI_3$ is more positive than that of BP so that photo-generated h^+ could also migrate from $MAPbI_3$ to BP, where the I_3^- oxidized by I^- can be consumed by H_3PO_2. As a consequence, the photogenerated electrons and holes can be effectively separated, which can largely promote the photocatalytic HER activity of the $BP/MAPBI_3$ heterostructure composite. Worthy noted, we checked the concentrations of I^- prior to and after the photocatalysis, the determined concentrations of iodine ions in two cases are almost the same value i.e. ~ 7.43 mol L^{-1}, illustrating no change of I^- ion during the photocatalysis. This result also may confirm the reduction of I_3^- to I^- mediated by H_3PO_2.

4. Conclusions

A highly efficient and stable heterostructured $BP/MAPbI_3$ has been synthesized and implemented as a photocatalyst for splitting HI to produce H_2. The fabricated 1.2% $BP/MAPbI_3$ photocatalyst shows a superb visible-light photocatalytic HER rate of 3742 µmol h^{-1} g^{-1} in $MAPbI_3$-saturated HI solution, much higher than that of pure $MAPbI_3$. Such a HER rate also outstrips all reported perovskite-based photocatalysts. Furthermore, the $BP/MAPbI_3$ photocatalyst shows excellent photocatalytic stability in the process of the whole photoreaction. The outstanding photocatalytic performances of the $BP/MAPbI_3$ including HER evolution and stability in aqueous HI solution can be originated from the following aspects of reasons: i) broadened light harvesting by introducing BP; ii) improved charge carrier separation/transport at the interface of $BP/MAPbI_3$; and iii) high chemical/optical stability of $BP/MAPbI_3$ heterostructure in HI solution. This work may open up new opportunities for reliably synthesizing high efficiency and stable organic-inorganic perovskite-based photocatalysts by combining 2D cocatalyst for improving their performances in photocatalysis.

Declaration of Competing Interest

The authors declare that they have no known competing financial interests or personal relationships that could have appeared to influence the work reported in this paper.

Acknowledgements

Appendix A. Supplementary data

Supplementary material related to this article can be found, in the online version, at doi:https://doi.org/10.1016/j.apcatb.2019.118075.

References

[1] R. Jingrun, Z. Jun, Y. Jiaguo, J. Mietek, Q. Shi Zhang, Chem. Soc. Rev. 46 (2015) 7787–7812.
[2] Z. Xiaoxin, Z. Yu, Chem. Soc. Rev. 44 (2015) 5148–5180.
[3] T.P. Yoon, M.A. Ischay, J. Du, Nat. Chem. 2 (2010) 527.
[4] A.A. Ismail, D.W. Bahnemann, Sol. Energy Mater. Sol. Cells 128 (2014) 85–101.
[5] T. Hisatomi, J. Kubota, K. Domen, Chem. Soc. Rev. 43 (2014) 7520–7535.
[6] J. Ran, T.Y. Ma, G. Gao, X.-W. Du, S.Z. Qiao, Energy Environ. Sci. 8 (2015) 3708–3717.
[7] C. Eames, J.M. Frost, P.R. Barnes, B.C. O'Regan, A. Walsh, M.S. Islam, Nat. Commun. 6 (2015) 7497.
[8] I. Jeong-Hyeok, J. In-Hyuk, P. Norman, G.T. Michael, P. Nam-Gyu, Nanotechnology 9 (2014) 927–932.
[9] L. Zhu, J. Xiao, J. Shi, J. Wang, S. Lv, Y. Xu, Y. Luo, Y. Xiao, S. Wang, Q. Meng, Nano Res. 8 (2015) 1116–1127.
[10] X. Li, M.I. Dar, C. Yi, J. Luo, M. Tschumi, S.M. Zakeeruddin, M.K. Nazeeruddin, H. Han, M. Grätzel, Nat. Chem. 7 (2015) 703–711.
[11] A. Kojima, K. Teshima, Y. Shirai, T. Miyasaka, J. Am. Chem. Soc. 131 (2009) 6050–6051.
[12] L. Mingzhen, M.B. Johnston, H.J. Snaith, Nature 501 (2013) 395.
[13] J. Ding, Z. Lian, Y. Li, S. Wang, Q. Yan, J. Phys. Chem. Lett. 9 (2018) 4221–4226.
[14] S. Park, W.J. Chang, W.L. Chan, S. Park, H.Y. Ahn, K.T. Nam, Nat. Energy 2 (2016) 16185.
[15] Y. Wu, P. Wang, X. Zhu, Q. Zhang, Z. Wang, Y. Liu, G. Zou, Y. Dai, M.H. Whangbo, B. Huang, Adv. Mater. 30 (2018) 1704342.
[16] X. Wang, W. Hong, H. Zhang, Y. Wei, X. Wang, Z. Yue, Z. Xu, C. Li, ACS Energy Lett. 3 (2018) 1159–1164.
[17] S. Cao, J. Yu, J. Phys. Chem. Lett. 5 (2014) 2101–2107.
[18] B. Sa, Y.-L. Li, J. Qi, R. Ahuja, Z. Sun, J. Phys. Chem. Lett. 118 (2014) 26560–26568.
[19] L. Kou, C. Chen, S.C. Smith, J. Phys. Chem. Lett. 6 (2015) 2794–2805.
[20] A. Castellanos-Gomez, J. Phys. Chem. Lett. 6 (2015) 4280–4291.
[21] J. Hu, Z. Guo, P.E. McWilliams, J.E. Darges, D.L. Druffel, A.M. Moran, S.C. Warren, Nano Lett. 16 (2016) 74–79.
[22] M.Z. Rahman, C.W. Kwong, K. Davey, S.Z. Qiao, Energy Environ. Sci. 9 (2016) 709–728.
[23] A.H. Woomer, T.W. Farnsworth, J. Hu, R.A. Wells, C.L. Donley, S.C. Warren, ACS Nano 9 (2015) 8869–8884.
[24] M. Zhu, S. Kim, L. Mao, M. Fujitsuka, J. Zhang, X. Wang, T. Majima, J. Am. Chem. Soc. 139 (2017) 13234–13242.
[25] M. Zhu, Z. Sun, M. Fujitsuka, T. Majima, Angew. Chem. Int. Ed. 57 (2018) 2160–2164.
[26] R. He, J. Hua, A. Zhang, C. Wang, J. Peng, W. Chen, J. Zeng, Nano Lett. 17 (2017) 4311–4316.
[27] A. Carvalho, M. Wang, X. Zhu, A.S. Rodin, H. Su, A.H. Castro Neto, Nat. Rev. Mater. 1 (2016) 16061.
[28] L. Bai, L. Sun, Y. Wang, Z. Liu, Q. Gao, H. Xiang, H. Xie, Y. Zhao, J. Mater. Chem. A 5 (2017) 8280–8286.
[29] Y. Yang, J. Gao, Z. Zhang, S. Xiao, H.H. Xie, Z.B. Sun, J.H. Wang, C.H. Zhou, Y.W. Wang, X.Y. Guo, Adv. Mater. 28 (2016) 8787-8787.
[30] X. Cai, L. Mao, S. Yang, K. Han, J. Zhang, ACS Energy Lett. 3 (2018) 932–939.
[31] J. Ran, B. Zhu, S. Qiao, Angew. Chem. Int. Ed. 56 (2017) 10373–10377.
[32] X. Zhu, T. Zhang, Z. Sun, H. Chen, J. Guan, X. Chen, H. Ji, P. Du, S. Yang, Adv. Mater. 29 (2017) 1605776.
[33] A. Ambrosi, Z. Sofer, M. Pumera, Angew. Chem. Int. Ed. 56 (2017) 10443–10445.
[34] Y. Wang, H.B. Fang, Y.Z. Zheng, R. Ye, X. Tao, J.F. Chen, Nanoscale 7 (2015) 19118–19128.
[35] M. Zhu, C.Y. Zhai, M. Fujitsuka, T. Majima, Appl. Catal. B: Environ. 221 (2018) 645–651.
[36] Z. Guo, H. Zhang, S. Lu, Z. Wang, S. Tang, J. Shao, Z. Sun, H. Xie, H. Wang, X.-F. Yu, P.K. Chu, Adv. Funct. Mater. 25 (2015) 6996–7002.
[37] Y. Huang, J. Qiao, K. He, S. Bliznakov, E. Sutter, X. Chen, D. Luo, F. Meng, D. Su, J. Decker, W. Ji, R.S. Ruoff, P. Sutter, Chem. Mater. 28 (2016) 8330–8339.
[38] H.-B. Fang, X.-H. Zhang, J. Wu, N. Li, Y.-Z. Zheng, X. Tao, Appl. Catal. B: Environ. 225 (2018) 397–405.
[39] N. Li, J. Wu, Y. Lu, Z. Zhao, H. Zhang, X. Li, Y.-Z. Zheng, X. Tao, Appl. Catal. B: Environ. 238 (2018) 27–37.
[40] H. Wang, X. Wang, R. Chen, H. Zhang, X. Wang, J. Wang, J. Zhang, L. Mu, K. Wu, F. Fan, X. Zong, C. Li, ACS Energy Lett. 4 (2018) 40–47.
[41] Z. Zhao, J. Wu, Y.-Z. Zheng, N. Li, X. Li, Z. Ye, S. Lu, X. Tao, C. Chen, Appl. Catal. B: Environ. 253 (2019) 41–48.
[42] M. Zhu, Y. Osakada, S. Kim, M. Fujitsuka, T. Majima, Appl. Catal. B: Environ. 217 (2017) 285–292.
[43] J. Lin, P. Wang, H. Wang, C. Li, X. Si, J. Qi, J. Cao, Z. Zhong, W. Fei, J. Feng, Adv. Sci. 6 (2019) 1900246.
[44] B. Tang, Z.G. Yu, H.L. Seng, N. Zhang, X. Liu, Y.W. Zhang, W. Yang, H. Gong, Nanoscale 10 (2018) 20113–20119.
[45] K. He, J. Xie, Z.-Q. Liu, N. Li, X. Chen, J. Hu, X. Li, J. Mater. Chem. A 6 (2018) 13110–13122.
[46] S. Ma, Y. Deng, J. Xie, K. He, W. Liu, X. Chen, X. Li, Appl. Catal. B: Environ. 227 (2018) 218–228.
[47] B. Han, S. Liu, N. Zhang, Y.-J. Xu, Z.-R. Tang, Appl. Catal. B: Environ. 202 (2017) 298–304.
[48] R. Boppella, W. Yang, J. Tan, H.-C. Kwon, J. Park, J. Moon, Appl. Catal. B: Environ. 242 (2019) 422–430.
[49] F.X. Xiao, S.F. Hung, J. Miao, H.Y. Wang, H. Yang, B. Liu, Small 11 (2015) 554–567.
[50] M. Zhu, M. Fujitsuka, L. Zeng, M. Liu, T. Majima, Appl. Catal. B: Environ. 256 (2019) 117864.
[51] J. Hu, D. Chen, Z. Mo, N. Li, Q. Xu, H. Li, J. He, H. Xu, J. Lu, Angew. Chem. Int. Ed. 58 (2019) 2073–2077.
[52] X.L. Yin, L.L. Li, W.J. Jiang, Y. Zhang, X. Zhang, L.J. Wan, J.S. Hu, ACS Appl. Mater. Interfaces 8 (2016) 15258–15266.
[53] Q. Zhao, J. Sun, S. Li, C. Huang, W. Yao, W. Chen, T. Zeng, Q. Wu, Q. Xu, ACS Catal. 8 (2018) 11863–11874.
[54] Q. Chen, H. Zhou, T.B. Song, S. Luo, Z. Hong, H.S. Duan, L. Dou, Y. Liu, Y. Yang, Nano Lett. 14 (2014) 4158–4163.
[55] M.Q. Yang, Y.J. Xu, W. Lu, K. Zeng, H. Zhu, Q.H. Xu, G.W. Ho, Nat. Commun. 8 (2017) 14224.
[56] N. Li, J. Wu, H.-B. Fang, X.-H. Zhang, Y.-Z. Zheng, X. Tao, Appl. Surf. Sci. 448 (2018) 41–49.
[57] H. Yu, R. Shi, Y. Zhao, T. Bian, Y. Zhao, C. Zhou, G.I.N. Waterhouse, L.Z. Wu, C.H. Tung, T. Zhang, Adv. Mater. 29 (2017) 1605148.
[58] Q. Liang, F. Shi, X. Xiao, X. Wu, K. Huang, S. Feng, ChemCatChem 10 (2018) 2179–2183.
[59] W. Wang, G. Li, T. An, D.K.L. Chan, J.C. Yu, P.K. Wong, Appl. Catal. B: Environ. 238 (2018) 126–135.
[60] X. Li, X. Lv, N. Li, J. Wu, Y.-Z. Zheng, X. Tao, Appl. Catal. B: Environ. 243 (2019) 76–85.
[61] B. Qiu, Q. Zhu, M. Xing, J. Zhang, Chem. Commun. 53 (2017) 897–900.